



Gust load alleviation by normal microjet

Yonghong Li ^{a,b}, Ning Qin ^{a,*}

^a Department of Mechanical Engineering, The University of Sheffield, Sheffield S1 3JD, UK

^b High Speed Aerodynamic Institute, China Aerodynamic Research and Development Center, Mianyang 621000, China

ARTICLE INFO

Article history:

Received 10 March 2021

Received in revised form 16 April 2021

Accepted 22 June 2021

Available online 8 July 2021

Communicated by Mehdi Ghoreyshi

Keywords:

Gust load alleviation

Normal microjet

Blowing momentum

Reduced frequency

BAH wing

ABSTRACT

This paper presents an investigation on the capability of gust load alleviation by normal microjet. The numerical method integrates the unsteady Reynolds averaged Navier-Stokes (URANS) solutions, structural dynamic equations of motion and the Field Velocity Method. The method is verified for gust responses of rigid and elastic models. The numerical results of microjet are validated against experimental and previous numerical data. Load control capabilities of normal microjet are evaluated on the 2D NACA0012 airfoil and the 3D BAH wing with constant and dynamic momentum coefficients under steady subsonic and transonic incoming flow conditions. Thereafter, gust load alleviation effects using microjet are tested on the airfoil and the BAH wing with and without the consideration of aeroelasticity. The results show that normal microjet has a strong capability for load control for transonic incoming flow. This is due to the jet effect on the shock strength on the airfoil upper surface. For the 3D BAH wing, significant load control effects can be shown for jet deployment on the span near the wing tip. Load reduction has also been observed near the wing root away from the jet region. The test cases show that normal microjet is a promising approach for gust load alleviation with a fast frequency response characteristic. A near constant lift response under gust condition can be achieved by adaptively adjusting the blowing momentum coefficients.

© 2021 Elsevier Masson SAS. All rights reserved.

1. Introduction

Gust loads are of critical importance to civil transport aircraft design, often determining the maximum loads and the mass of the aircraft structure. For aircraft design, a large number of gust load cases need to be considered, requiring expensive test data. There is a strong interest in the recent years on alternative ways for reliable gust load predictions. For example, a resent collaborative research project between industry and academia named AeroGust [1] (Aeroelastic Gust Modeling) has been carried out to investigate and develop numerical methods for gust simulations.

With gust load prediction, gust load control and alleviation can be investigated for design of safer aircraft. Most research activities have been on the design of gust load alleviation systems especially on the design of control laws, such as the linear quadratic regulator theory [2], linear quadratic Gaussian method [3], and a novel model predictive control approach based on the nonlinear Hammerstein model [4]. Effective gust control depends heavily on the response time of the control means. Control surfaces comprising of ailerons and spoilers have been used for gust load alleviation.

However, these control surfaces are often sized for maneuvers, and therefore exhibit low-frequency response due to their large inertia [5]. Al-Battal [6] pointed out that these control surfaces become ineffective for alleviating high-frequency gusts. Therefore, it is important to investigate fast response actuators for gust load alleviation. In addition, being able to fly and control aircraft without conventional control surfaces (namely flapless control) is one of the targets for future aircraft design with benefits including fewer moving parts, possibly less weight, less maintenance and enhanced stealth characteristics [7]. One of the promising methods to replace these traditional flaps is to employ fluidic actuators.

As a means for active aerodynamic flow control, fluidic actuators have been investigated for many decades, including synthetic jets, circulation control using Coanda effects, and steady blowing and suction. These methods have been shown to be effective for aerodynamic improvements, such as drag reduction [8,9], delay of transition [10,11], flow separation control [12–14], and stall control and lift augmentation [15,16]. Similar to lift augmentation, fluidic actuators are also capable to reduce and manage lift, which provides a potential way for gust load attenuation. Some initial studies have been conducted recently to evaluate the effects of fluidic actuators for reducing lift. Boeije et al. [17] reported an experimental and numerical study of a normal jet placed near an airfoil trailing edge on the upper surface, showing an effective reduction of lift.

* Corresponding author.

E-mail address: n.qin@sheffield.ac.uk (N. Qin).

Nomenclature

s	non-dimensional time	M	Mach number
C_{mx}	wing root bending moment coefficient	α	angle of attack
C_L	lift coefficient	U_∞	freestream velocity
w_g	gust velocity	C_p	pressure coefficient
w_{g0}	peak velocity of 'one-minus-cosine' gusts	c	chord length
H_g	gust wavelength	\bar{c}	mean aerodynamic chord length
C_μ	momentum coefficient	$Re_{\bar{c}}$	Reynolds number
$C_{\mu 0}$	peak momentum coefficient	x, y, z	Cartesian coordinates in streamwise, spanwise and vertical directions
k	reduced frequency		

More recently, Al-Battal et al. [5,18] conducted further experimental investigation to compare the lift reduction capabilities between normal and counter jets. Rao et al. [19] studied aeroelastic response controls of flutter and limit cycle oscillation using synthetic jet on the NACA 0015 airfoil. Blaylock et al. [20]'s numerical study compared load control effectiveness of microjets and mini-tabs deployed on the NACA0012 airfoil trailing edge. The results showed that both concepts had a similar load control mechanism by affecting the trailing-edge flow, and therefore produced very similar aerodynamic load control effects. Heathcote et al. [21] gave further insight in comparing the effects of microjets and mini-tabs by wind tunnel tests and pointed out that blowing and mini-tabs were viable methods for load control but with very different behaviors. The blowing deflected the wake upwards thereby reducing lift. Conversely, the mini-tabs promoted separation over the upper surface. They also noted that the lift change by microjet located at the trailing edge is nearly constant for different angle of attacks, which was consistent with the result drawn by de Vries et al. [17]. However, for mini-tabs, optimal location varied with the angle of attack. At low incidences, it is preferable to place the mini-tabs near the trailing edge, while locations near the leading edge were found to be better when the angle of attack is high.

Previous studies using microjets were conducted for constant incoming flow and therefore its ability to directly alleviate gust loads is still unknown. The motivation of this study is to explore novel method for gust load alleviation. The feasibility and effects of gust load alleviation by means of microjet perpendicular to wing upper surface is studied. Firstly, validation work on numerical methods including the simulations of gust and microjet has been done. Thereafter, load control effects of normal microjet with constant and dynamic actuators are studied. Finally, the gust load alleviation effects on the 2D NACA0012 airfoil and 3D BAH wing without and with the consideration of aeroelasticity are demonstrated.

2. Numerical methods

2.1. URANS solver

The numerical solver is the NASA Open CFD software CFL3D [22]. It is a multi-block structured upwind finite volume CFD code. The 3D time-dependent compressible Navier-Stokes equations can be expressed in an integral form as follows:

$$\frac{\partial}{\partial t} \iiint \mathbf{W} dV + \iint [\mathbf{F} - \mathbf{G}] \cdot d\mathbf{A} = 0 \quad (1)$$

where, t is the time, \mathbf{W} is the conserved variables; V is an arbitrary control volume; \mathbf{F} and \mathbf{G} are the inviscid and viscous fluxes, respectively; $d\mathbf{A}$ is the vector of the differential surface area.

The variables and the fluxes are

$$\mathbf{W} = \begin{bmatrix} \rho \\ \rho v_x \\ \rho v_y \\ \rho v_z \\ e \end{bmatrix}, \quad F = \begin{bmatrix} \rho \mathbf{v} \\ \rho \mathbf{v} v_x + p \hat{i} \\ \rho \mathbf{v} v_y + p \hat{j} \\ \rho \mathbf{v} v_z + p \hat{k} \\ (e + p) \mathbf{v} \end{bmatrix}, \quad G = \begin{bmatrix} 0 \\ \boldsymbol{\tau}_{xi} \\ \boldsymbol{\tau}_{yi} \\ \boldsymbol{\tau}_{zi} \\ \boldsymbol{\tau}_{ij} v_j - \mathbf{q} \end{bmatrix}$$

where, ρ , p , e , and \mathbf{v} are the density, pressure of the fluid, total energy per unit volume, and velocity, respectively. $\boldsymbol{\tau}_{ij}$ is shear stress, and \mathbf{q} is the heat flux.

For the convective terms, a 3rd order upwind-biased spatial differencing (Roe scheme) is used, and the viscous terms are discretized by second-order central differencing. For the turbulence model, k- ω SST model is used in this study.

CFL3D has the capability to perform both static and dynamic aeroelastic analysis. CFL3D performs aeroelastic analysis by solving the aeroelastic equations of motion in the generalized modal state space as:

$$\mathbf{M} \ddot{\mathbf{q}} + \mathbf{C} \dot{\mathbf{q}} + \mathbf{K} \mathbf{q} = \mathbf{Q}, \quad q^T = [q_1, q_2 \dots] \quad (2)$$

where \mathbf{q} is generalized displacement vector; \mathbf{K} is generalized stiffness matrix; \mathbf{C} is generalized damping matrix; \mathbf{M} is the generalized mass matrix, and \mathbf{Q} is generalized force.

The time matching of the fluid/structure coupling uses a second-order backward differencing and a predictor/corrector scheme, which can be found in Ref. [23] for more details. Prior to running the CFL3D code for fluid-structural calculations, frequencies, generalized masses, and mode shapes should be provided and projected onto the grid points of the computational model surface.

2.2. Gust treatment by field velocity method

The gust perturbations is implemented in the computational domain using the Field Velocity Method (FVM) proposed by Parameswaran et al. [24,25], in which the prescribed gust velocity is introduced into the grid velocities as:

$$v_{grid}[(x, y, z), t] \rightarrow v_{grid}[(x, y, z), t] - v_{gust}[(x, y, z), t] \quad (3)$$

Based on the *dynamic mesh module* in CFL3D, the functions based on FVM were added in the code with the capability to simulate arbitrary gust shapes.

3. Validation and verifications

For gust response simulations, the FVM method is integrated into the URANS solutions, which was verified by the authors in Ref. [26]. The numerical responses of a series of gust profiles including a step-change in the angle of attack, sharp-edged gusts and the one-minus-cosine gusts using the 2D rigid NACA0012 airfoil are compared to the Wagner function [27], Küssner function [28]

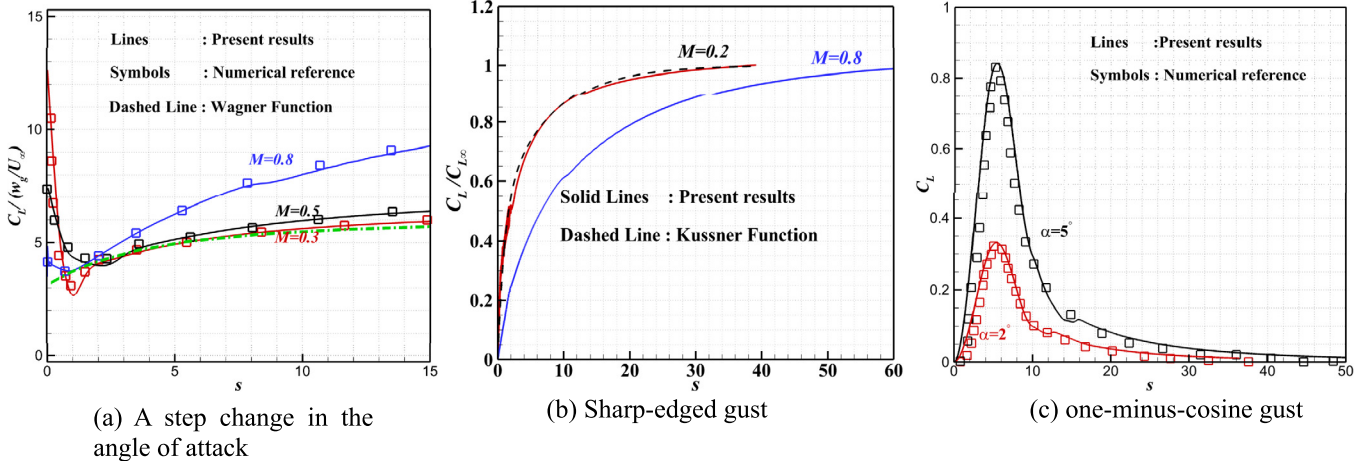


Fig. 1. Verification of the gust response simulations.

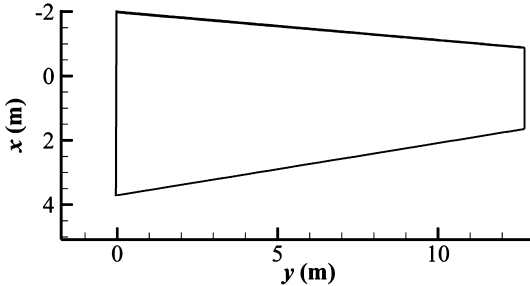


Fig. 2. Planform of the BAH wing.

and reference data from Ref. [29], respectively. Some comparisons are presented in Fig. 1 and further details can be found in Ref. [26].

To consider the aeroelasticity and rigid motions in gust response, additional validation work is carried out using the 3D BAH wing with the plunging and the first bending modes. The solver coupling URANS solutions, structural dynamic equations of motion and FVM are validated through the comparison between the present numerical results and the available data as presented in the following section.

3.1. Verification of the gust response of the elastic BAH wing

The BAH wing is a jet transport aircraft test wing, on which Bisplinghoff et al. [30] conducted comprehensive investigations in the area of aeroelasticity. The BAH wing is a half wing with a wingspan $l = 12.7$ m, a mean aerodynamic chord $\bar{c} = 4.1275$ m, and a wing area $S = 52.42$ m². The BAH wing planform is shown in Fig. 2.

A wide range of aeroelastic test cases have been previously validated using the commercial software, MSC/NASTRAN [31], with high-fidelity structural analysis as reported in [32]. The BAH wing has been adopted by Rodden et al. [33] as an MSC/NASTRAN demonstration problem in random gust response analysis. In MSC/NASTRAN, the aerodynamic force is determined by the Doublet Lattice Method [34] ignoring the wing-section thickness effects. To compare with the MSC/NASTRAN data, the NACA65A004 airfoil is used here to construct the CFD model of the BAH wing. The mesh topology of the computational domain is shown in Fig. 3 and the total grid size is about 4.0×10^6 .

The mode shapes are extracted from the structural model in MSC/NASTRAN and are projected to the grid points on the wing surface of the CFD model. In this study, two typical modes are included in the simulation. The first is the plunging mode and the second is the first bending elastic mode with a natural frequency of 2.44 Hz. The mode shape profiles are shown in Fig. 4.

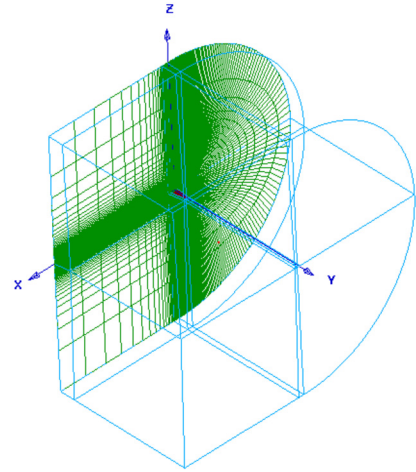


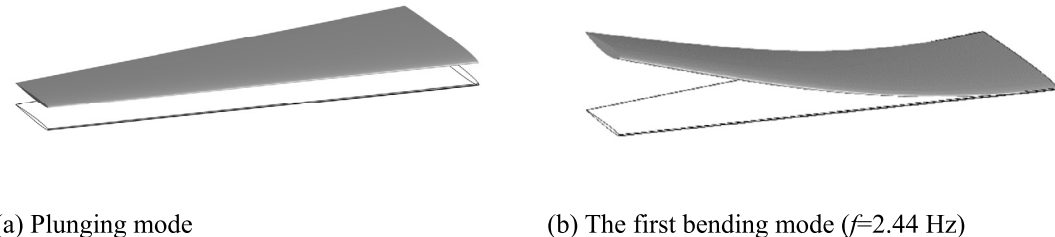
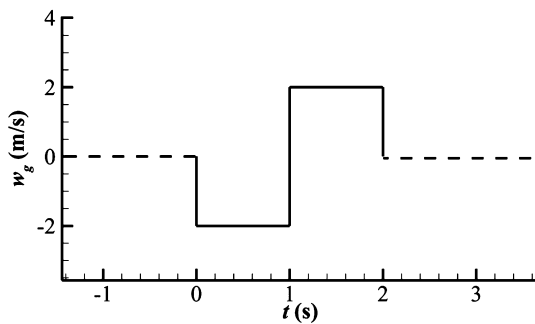
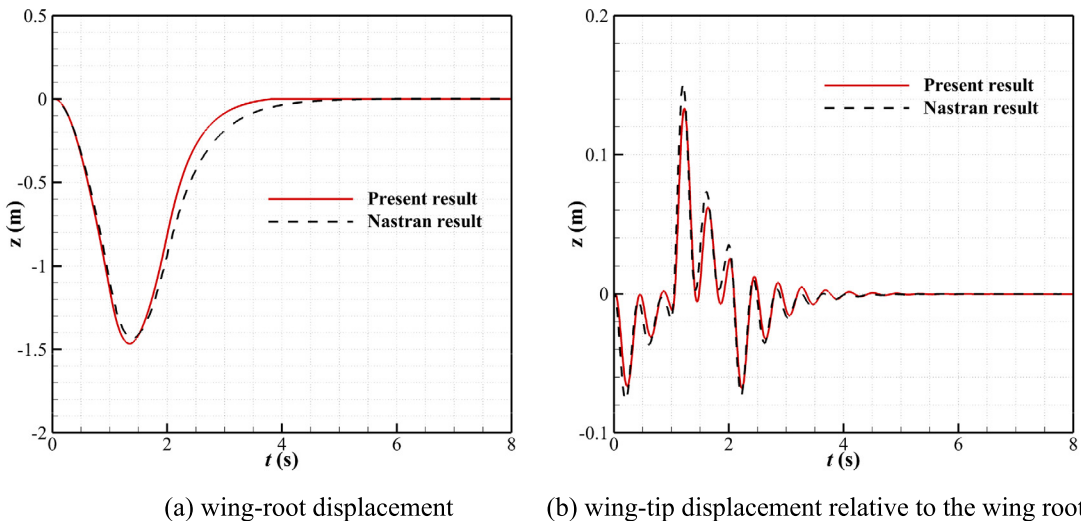
Fig. 3. Mesh topology of the BAH wing.

In MSC/NASTRAN, the demonstration case calculates the time history of the displacement responses of the BAH wing due to a gust load. The gust is a square wave gust shown in Fig. 5 with a duration of 2 seconds. The freestream Mach number is 0.62 and the gust amplitude w_g is taken as 0.01 times the incoming flow velocity at 2 m/s.

The square wave gust is assigned to the grid points of the CFD domain based on FVM. Fluid and structure are coupled in the present numerical solver as described in Section 2. Responses of the fluid-structure interactions of the BAH wing under this square wave gust is calculated by the present numerical solver. The vertical displacement responses are compared with the MSC/NASTRAN results [31] shown in Fig. 6. As shown in the comparison, the present results agree well with that calculated by MSC/NASTRAN, which indicates that apart from rigid models verified in detail in [26], the present solver is capable of and accurate for gust response simulations of elastic models with motions.

3.2. Validation for normal microjet

Eggert et al. [35] evaluated RANS using CFL3D code to predict the effects of active flow control by blowing from the leading-edge slot on the NACA 0018 airfoil. In that study, the jet slots pointed at a 20° toward the trailing edge of the airfoil and the freestream Mach number of 0.03265. CFL3D code using RANS predicted similar flow characteristics to those present in the experimental data. To validate the current methodology for normal microjet, the nu-

**Fig. 4.** The mode shape profiles of the BAH wing.**Fig. 5.** The profile of the square wave gust.**Fig. 6.** Comparison of the real displacement responses.

merical and experimental results conducted by de Vries et al. [17] are applied for the comparisons. The studies were conducted based on the NACA0018 airfoil with microjet placing at $x/c = 0.9$.

To model jet blowing, Blaylock et al. [20] compared three different models: surface jets with constant velocities, surface jets with parabolic velocity profiles and jets created by plenums. The results showed close aerodynamic coefficients among these three models. This finding is consistent to the studies conducted by Rumsey [36] that the differences in aerodynamic coefficients between jets produced through plenums and jets generated from the surfaces are insignificant. Therefore, jets originating from airfoil or wing surfaces are used in this study.

The experimental model used by de Vries et al. [17] has $c = 0.165$ m; jet width $h_{jet} = 0.001$ m placed at $x/c = 0.9$ on the NACA0018 airfoil lower surface. The freestream properties are $M_\infty = 0.176$, $Re_c = 6.6 \times 10^5$. The blowing velocity is $1.2U_\infty$. The pressure was only measured at four points on the airfoil surface. de

Vries et al. [17] also conducted numerical investigation using the commercial computational fluid dynamics software package ANSYS CFX 11.0. The total lift changes between the airfoils with and without microjet under the same incoming flow condition as the experiment were evaluated.

Fig. 7 gives the comparisons of the calculated pressure distributions on models with and without microjet to the experimental data from Ref. [17]. The comparison shows a good agreement, especially for pressures on the upper surface. Fig. 8 presents the comparisons of the changes of lift coefficients between the present results and the reference data. In general, these results show a good match for both the models with and without microjet. It is also clear that the lift coefficient augmentation $\Delta C_L \approx 0.4$ is obtained due to the microjet with $U_{jet} = 1.2U_\infty$. In general, the present solver can capture the aerodynamic changes caused by microjet, which can be used for the following load control and gust load alleviation studies.

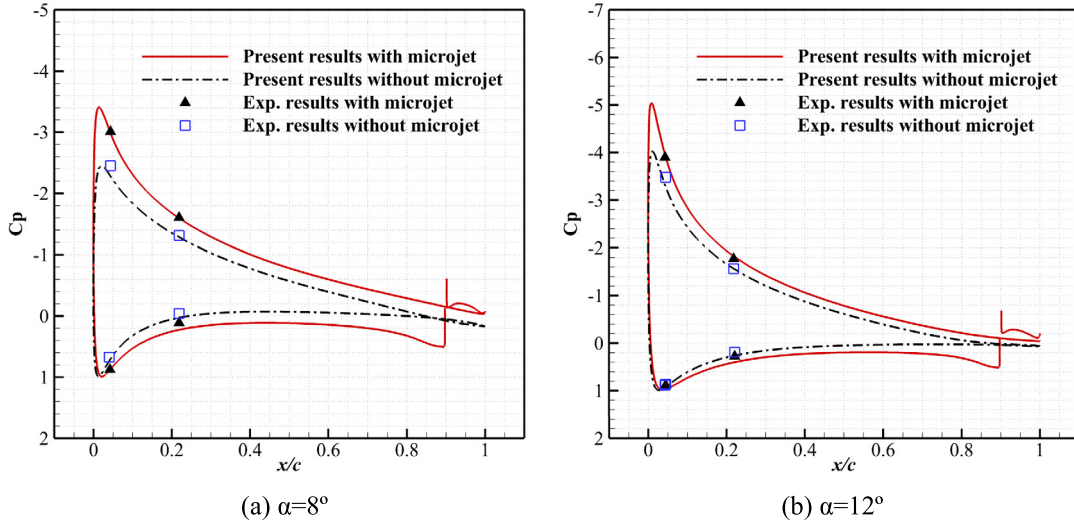


Fig. 7. Comparison of the pressure distribution of the NACA 0018 airfoil between the present results and the experimental results conducted by Boeije et al. [17].

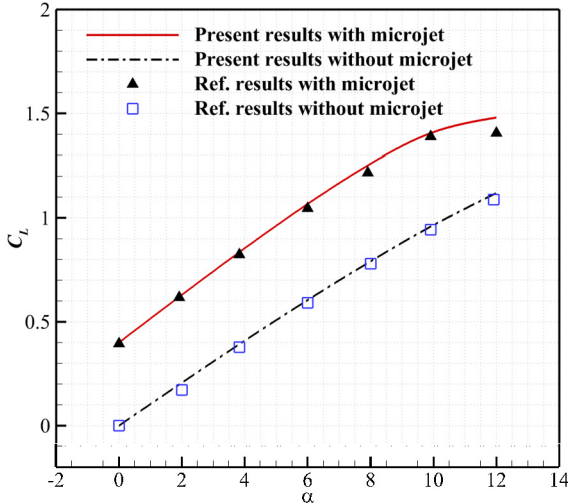


Fig. 8. Comparison of the lift coefficients of the NACA 0018 airfoil between the present results and the reference numerical results conducted by Boeije et al. [17].

4. Evaluation of load control capability under steady freestream conditions

4.1. NACA0012 airfoil

Al-Battal et al. [5] and Leopold [37] compared the efficiency of microjets placed on different chordwise locations on airfoils. Similar conclusions were obtained from those two studies that microjets placed on the trailing edge are more effective. Another important parameter about jet slot is the chordwise width, while there is little knowledge about its influence. Here, based on the NACA0012 airfoil, jets with slot width ranging from 0.2% c to 1.0% placed on $x/c = 0.95$ are compared under different blowing momentum coefficients to get a quantitative understanding of the influence of jet-slot width on the load control. Firstly, three different C-type grid resolutions are used to find an appropriate grid resolution for a coarse 221×121 mesh, a medium 321×141 mesh (as shown in Fig. 9, having 81 on the slot and the rest on the airfoil section), and a fine 421×161 mesh. These three grid resolutions are conducted on the airfoil with slot-width of 0.5% at $x/c = 0.95$ and the first grid distance from the airfoil is kept constant to ensure $y^+ \sim 0(1)$. Fig. 10 shows the pressure coefficient distributions of the model with $M_{\text{jet}} = 0.2$ at $M_\infty = 0.3$, $\alpha = 3^\circ$ and the model

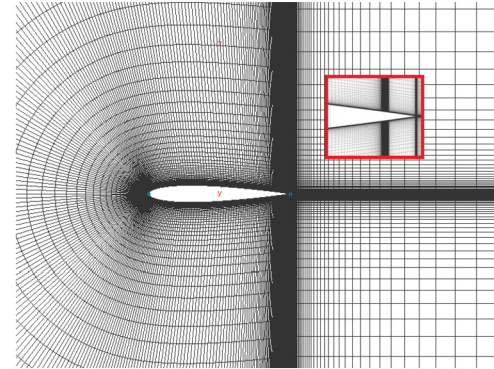


Fig. 9. NACA0012 airfoil with microjet at $x/c = 0.95$.

with $M_{\text{jet}} = 0.7$ at $M_\infty = 0.7$, $\alpha = 3^\circ$ for these three grid resolutions. The results show a negligible influence from the grid. The medium grid resolution is chosen.

Fig. 11(a) shows the results of lift reduction at $M_\infty = 0.3$, $\alpha = 0^\circ$ for different widths under the same blowing momentum coefficient of $C_\mu = 0.004$ and 0.009. In general, the magnitude of lift reduction increases with the increase of jet slot width. It is more obvious when the jet slot width is below 0.5% c , as the value of lift reduction tends to be stable when the slot width increases from 0.5% to 1.0% c for both $C_\mu = 0.004$ and 0.009. The trend is similar at $M_\infty = 0.7$, $\alpha = 0^\circ$ as shown in Fig. 11(b). A smaller width of the jet exit will be preferable from practical view point. Therefore, in the following studies, 0.5% is chosen for the slot width and $x/c = 0.95$ is chosen for the jet location.

To evaluate the load control effects, a series of computations with different momentum coefficients were conducted under $M_\infty = 0.3$ and $M_\infty = 0.7$ at $\alpha = 3^\circ$. The lift coefficient reduction with the increase of momentum coefficients is shown in Fig. 12. The maximum velocity of the microjet is set to be $1.5M_\infty$ before oscillations starts to appear. For the case with oscillation, the standard deviation is also shown in the results. The phenomenon of lift oscillation was also observed by Blaylock et al. [20] in the numerical study of normal microjet on NACA0012 airfoil. As shown in Fig. 12, normal microjet demonstrates a stronger load control capability at transonic speed than that in subsonic range.

Fig. 13 shows the evolutions of the Mach number contours and streamlines with the increase in blowing momentum coefficients at $M_\infty = 0.7$, $\alpha = 3^\circ$. Also shown is the region of interest around

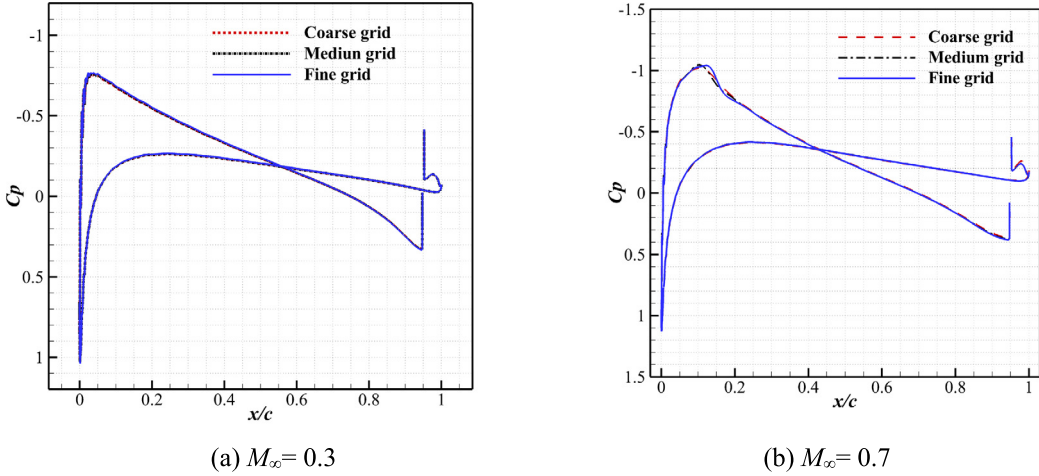


Fig. 10. Influence of grid resolutions on surface pressure distribution.

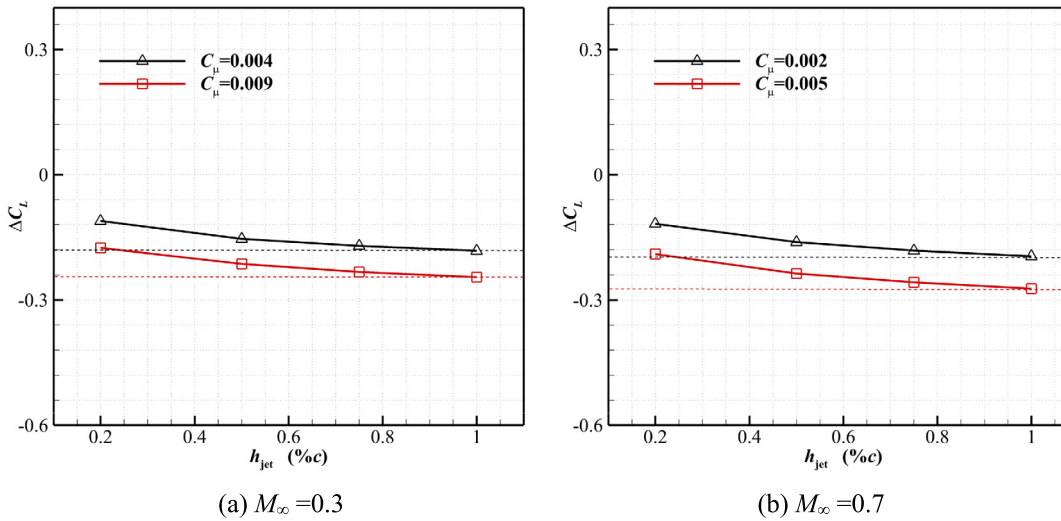


Fig. 11. Influence of jet slot width on lift coefficient at $\alpha = 0^\circ$.

the microjets near the trailing edge. As shown in the results, the high-speed jet flow presents itself as a blockage for the flow ahead the jet slot, thus decelerates the flow and increases the pressure coefficients on the upper surface as shown in Fig. 14. From the streamlines near the trailing edge of the blowing cases, it can be seen that the microjet not only deflects the streamlines above the upper surface but also entrains the flow from the lower surface upwards, which accelerates the flow resulting in a reduction in the pressure coefficients on the lower surface. If the external flow velocity is high, the blockage effects will significantly decelerate the external flow ahead the blowing location, thus has a stronger load control capability under transonic range. It is noticeable that when the momentum coefficient reaches a certain value, the shock wave is eliminated as can be seen from the pressure coefficient distributions of the model with $C_{\mu} = 9.65 \times 10^{-3}$. Behind the microjets, the pressure recovers rapidly due to the strong separation region formed behind the jet slot, which explains why it is more effective when jet slots are placed near the trailing edge.

4.2. BAH wing with microjet

On the BAH wing, the original NACA65A004 airfoil section is replaced by NACA0012 airfoil for having a reasonable thickness for jet application. As displayed in Ref. [30], the position of the aileron deployed on the BAH wing is from $\eta = y/b = 0.74$ (b stands for

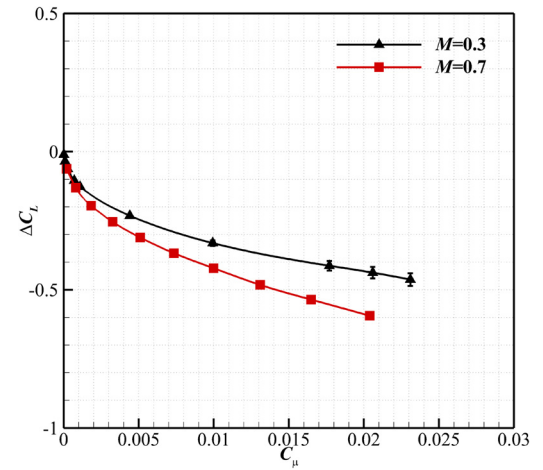


Fig. 12. Lift coefficient control effects on the 2-D airfoil.

the semi-span length) to the wingtip. Based on this information, a microjet slot with the same length in spanwise direction is included on the BAH wing as shown in Fig. 15. The slot is located on 95% of the local chord from the local leading edge with a slot width of 0.5% of the local chord.

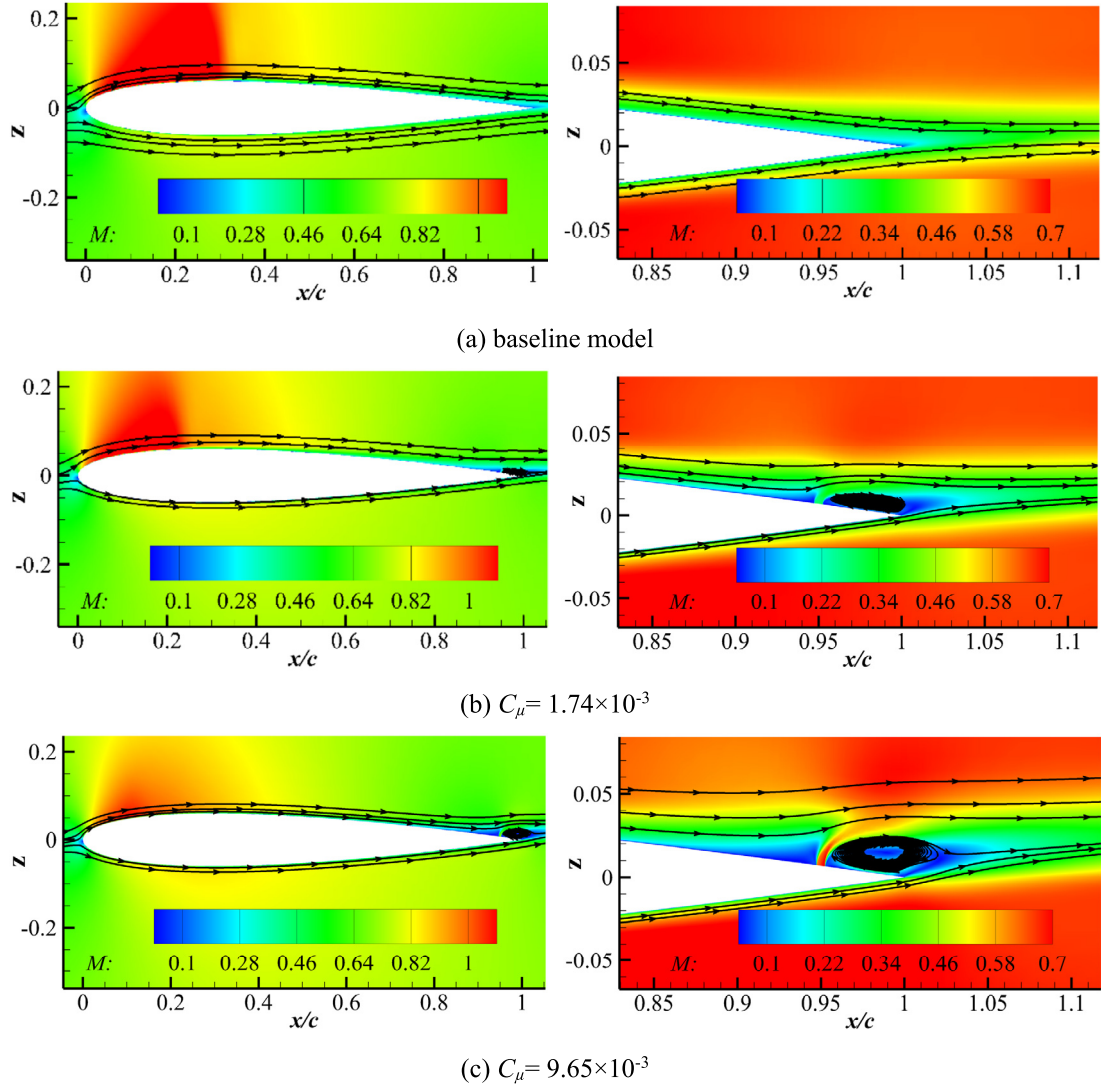


Fig. 13. Revolution of the Mach number contours and streamlines with increase in the blowing momentum coefficients at $M_\infty = 0.7$, $\alpha = 3^\circ$. (For interpretation of the colors in the figure(s), the reader is referred to the web version of this article.)

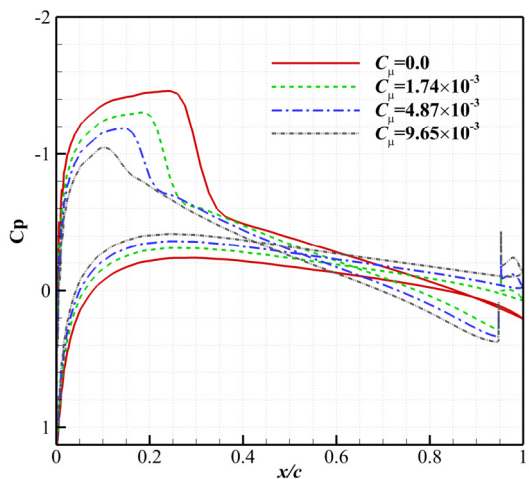


Fig. 14. Pressure coefficients distribution at $M_\infty = 0.7$, $\alpha = 3^\circ$.

Following the previous grid convergence study on the NACA0012 airfoil, a baseline grid with 321 cells (including 81 on the slot) on the wing airfoil section, 141 cells in the wall nor-

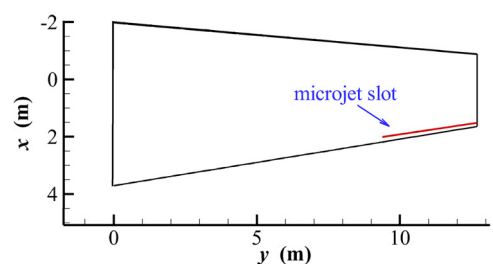


Fig. 15. The location of the microjet slot on the BAH wing.

mal direction and 121 cells along the span is generated. Through the airfoil grid influence study, it has been demonstrated that the number of cells on the airfoil section (321 cells) and the wall normal direction (141 cells) is enough to provide reasonably accurate results. Keeping the number of cells on these two directions, the number of cells along the spanwise direction is evaluated. From the baseline one with 121 cells over the span, a coarser grid with 81 cells and a finer grid with 161 cells are generated. Table 1 gives the effects of grid resolutions on the aerodynamic coefficients at $M_\infty = 0.7$, $\alpha = 3.0^\circ$ under a blowing momentum coefficient $C_\mu = 1.43 \times 10^{-4}$. It is noticeable that for the lift coefficient, the

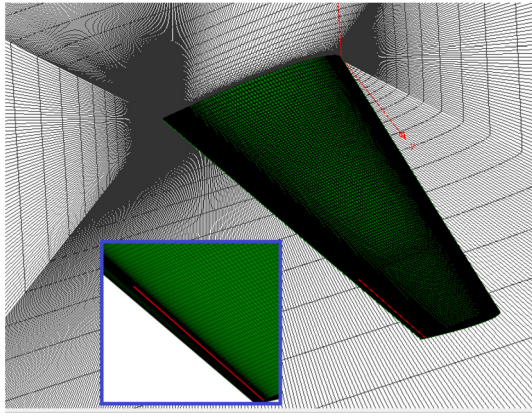


Fig. 16. Grid topology on the BAH wing with microjet slot.

Table 1

Grid resolution effects on aerodynamic coefficients of BAH wing with microjet slot ($M_\infty = 0.7$, $\alpha = 3.0^\circ$, $C_\mu = 3.58 \times 10^{-4}$).

Grid size	Coarse grid	Medium grid	Fine grid
C_L	0.2741	0.2755	0.2793
C_{mx}	0.1134	0.1140	0.1162

difference between the medium and the fine grids is less than 1.4%, and it is about 1.9% for the root bending moment coefficient. From these results, the medium grid is chosen in the following study. See also Fig. 16.

To get a quantitative understanding of the load control capability of normal microjet on the modified BAH wing, a series of computations with different momentum coefficients are conducted at $M_\infty = 0.3$, $\alpha = 3^\circ$, $Re_c = 4.13 \times 10^6$, and $M_\infty = 0.7$, $\alpha = 3^\circ$, $Re_c = 2.06 \times 10^7$, respectively. The maximum velocity for the microjet is also set to $M_{jet} = 1.5M_\infty$.

The reductions of lift coefficients due to normal microjet are compared in Fig. 17. It is consistent with the results on the airfoil that normal microjet blowing achieved stronger load control effect under transonic speed compared to that of subsonic range. Since microjet slot is only deployed on part of the span near the wing tip, it is worth to evaluate the influence of normal microjet on the whole spanwise load. The spanwise load distributions ($C_{L, local} * c/c_{ref}$) of the blowing cases are compared with the baseline model as shown in Fig. 18(a) for $M_\infty = 0.3$ and Fig. 18(b) for $M_\infty = 0.7$, respectively. For both Mach numbers, a more significant load control effect can be observed around microjet deployment region ($\eta = 0.74$ to 1.0). Apart from this region, load control effects are also shown on the spanwise loads towards the wing root where there is no jet blowing placement.

4.3. Time step resolutions and dynamic actuation of normal microjet

To successfully apply a microjet system for gust load alleviation, the performance under dynamic actuators is an important consideration. For the simulation of dynamic actuators, the influence of time step is evaluated under a transient actuation of microjet at $M_\infty = 0.3$, $\alpha = 3^\circ$ and $M_\infty = 0.7$, $\alpha = 3^\circ$, respectively. For this simulation, the BAH wing is initiated by the converged steady-state flow. Microjet is then activated at $s = 0$ to the maximum coefficient of $C_\mu = 1.28 \times 10^{-3}$ and $C_\mu = 2.9 \times 10^{-4}$ for $M_\infty = 0.3$ and 0.7 respectively. The non-dimensional time step Δs ranging from 7×10^{-4} to 7×10^{-3} is tested, and the results are shown in Fig. 19.

The results show that the differences in the lift responses from these three different time steps are negligible, especially between $\Delta s = 7 \times 10^{-4}$ and 1.4×10^{-3} . $\Delta s = 1.4 \times 10^{-3}$ is chosen here-

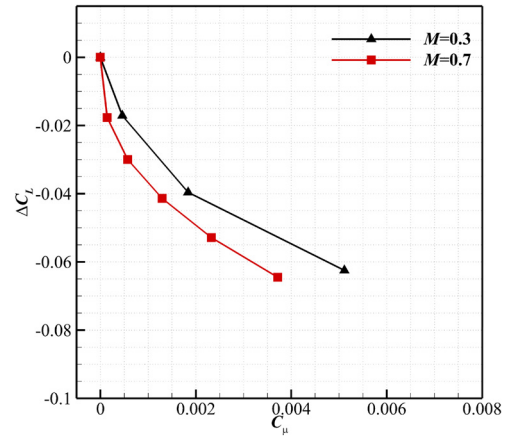


Fig. 17. Load control capability of under different Mach numbers.

after. The lift coefficients converge to the same final steady-state value generally at around $s = 10$ after activating the microjet. Also shown in the results is the sharp decrease of the lift coefficient at the first few non-dimensional time periods, indicating the fast response characteristic of microjet. More than 50% of the total change in lift coefficient has been obtained within $s = 1$. This is consistent with the results in [17] of the experimental and numerical study about the load control effects of surface jet on the NACA0018 airfoil at $M_\infty = 0.176$.

To understand the behavior of the dynamic actuators, the responses of microjet with periodic actuations are evaluated at $M_\infty = 0.3$ and 0.7 , $\alpha = 3^\circ$ respectively. The dynamic blowing momentum coefficient has the following form:

$$C_\mu = C_{\mu 0} \cdot |\sin(2\pi f \cdot s)| \quad (4)$$

The reduced frequency is $k = \pi f \bar{c} \bar{U}_\infty$. In EASA CS-25 [38], the typical gust length is defined as $12.5\bar{c}$, corresponding to a reduced frequency of 0.25. To assess the effects of microjet actuation frequency, three different reduced frequencies, i.e. $k = 0.125$, 0.25, 0.5, are tested with the maximum momentum coefficient $C_{\mu 0}$ of 1.28×10^{-3} and 2.9×10^{-4} for $M_\infty = 0.3$ and $M_\infty = 0.7$, respectively.

The results are shown in Fig. 20(a) in the forms of hysteresis loops for the lift responses against the changes in blowing momentum coefficient. All loops are clockwise. For these three blowing frequencies, the slopes are all negative, indicating effective increasing load control ability with increased blowing momentum coefficients. The slopes decrease slightly with the increased reduced frequency at both Mach numbers. This indicates the reduction of load control effects with the increase in blowing frequency.

5. Gust load alleviation

5.1. NACA0012 airfoil

'One-minus-cosine' gust is the typical discrete gust defined by the certification specifications of large commercial aircraft covered by EASA CS-25 [38]. To test normal microjet for gust load alleviation, the one-minus-cosine gust with gust velocity of $w_0/U_\infty = 0.066$ and wavelength of $11c$ is applied for the freestream flow condition of $M_\infty = 0.3$, $\alpha = 3^\circ$. At $s = 0$, the gust hits the airfoil leading edge and travels past the airfoil with the freestream velocity. Hence it takes $s = 12$ for the gust to pass the airfoil. The unsteady normal microjet with 'one-minus-cosine' profile in the time domain (see Eq. (5)) is tested. The peak momentum coefficients of $C_{\mu 0} = 1.1 \times 10^{-3}$ ($M_{jet} = 0.1$) and $C_{\mu 0} = 9.9 \times 10^{-3}$ ($M_{jet} = 0.3$) are applied for the two tested cases.

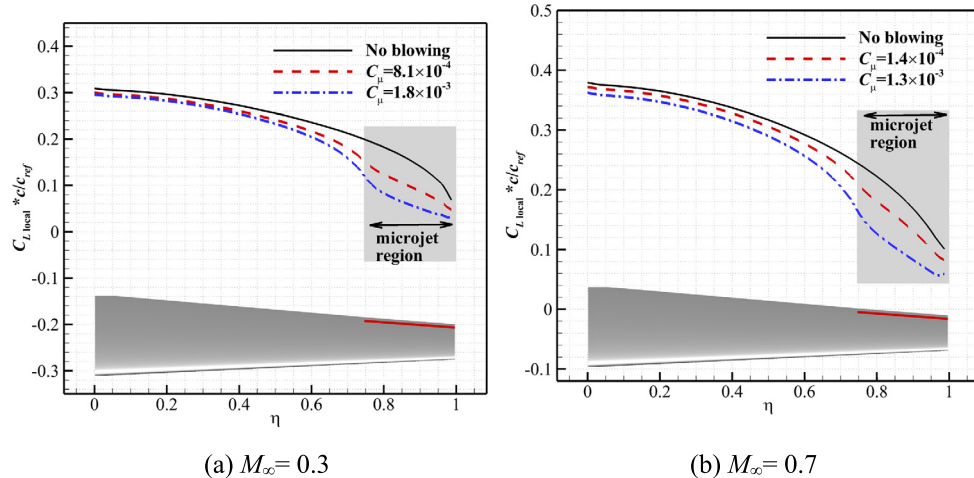


Fig. 18. Spanwise load distribution.

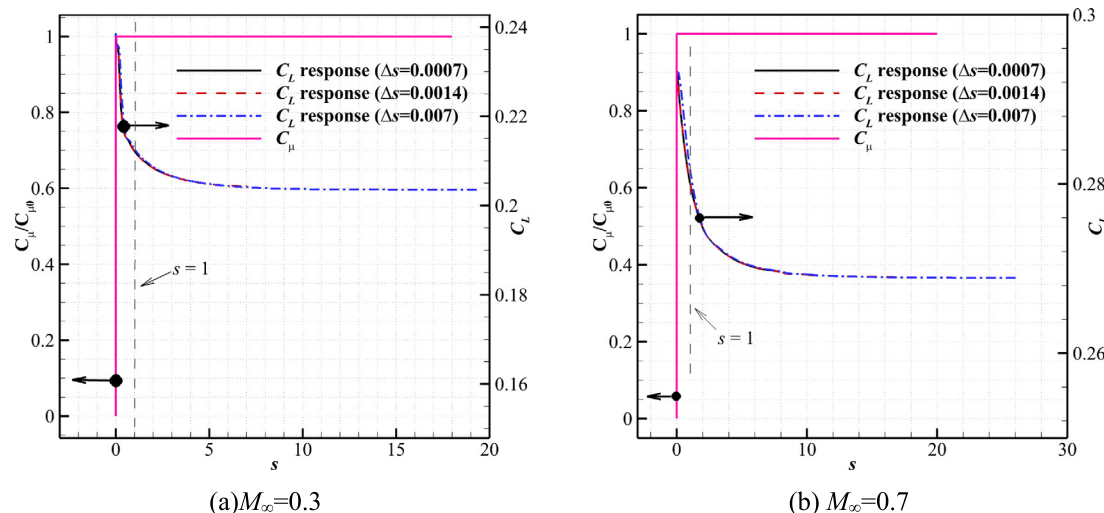


Fig. 19. Influence of the time steps.

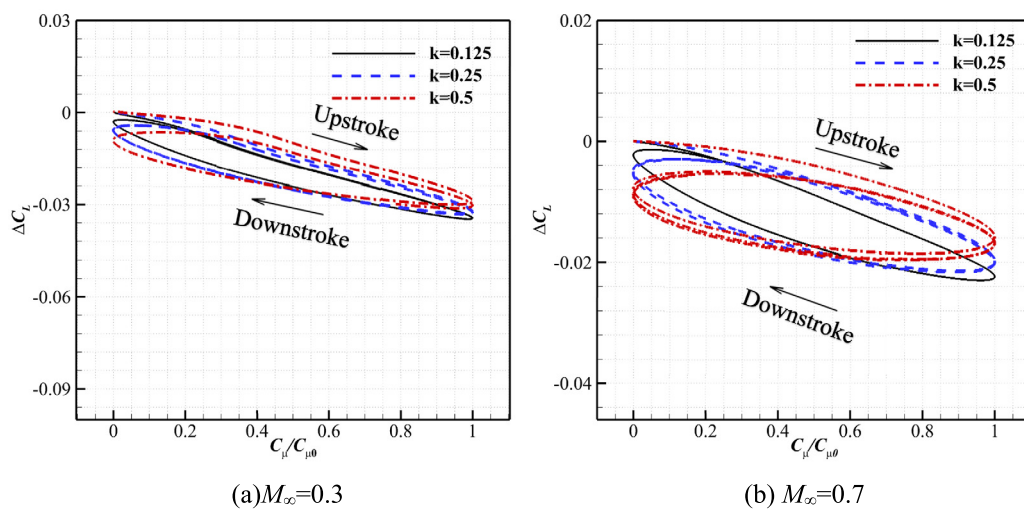


Fig. 20. Lift response with dynamic actuation of CC.

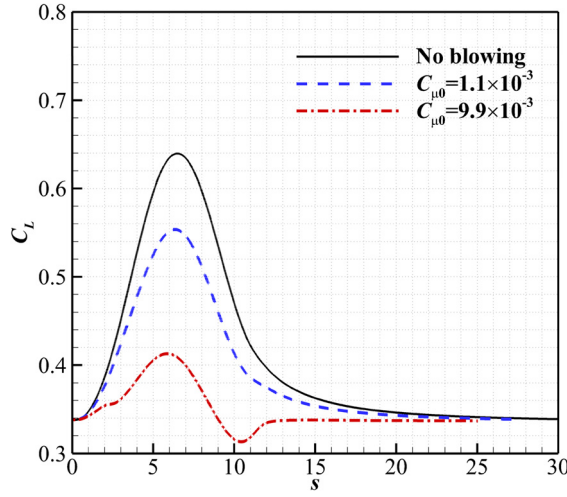


Fig. 21. The gust load alleviation by normal microjet blowing at $M_\infty = 0.3$.

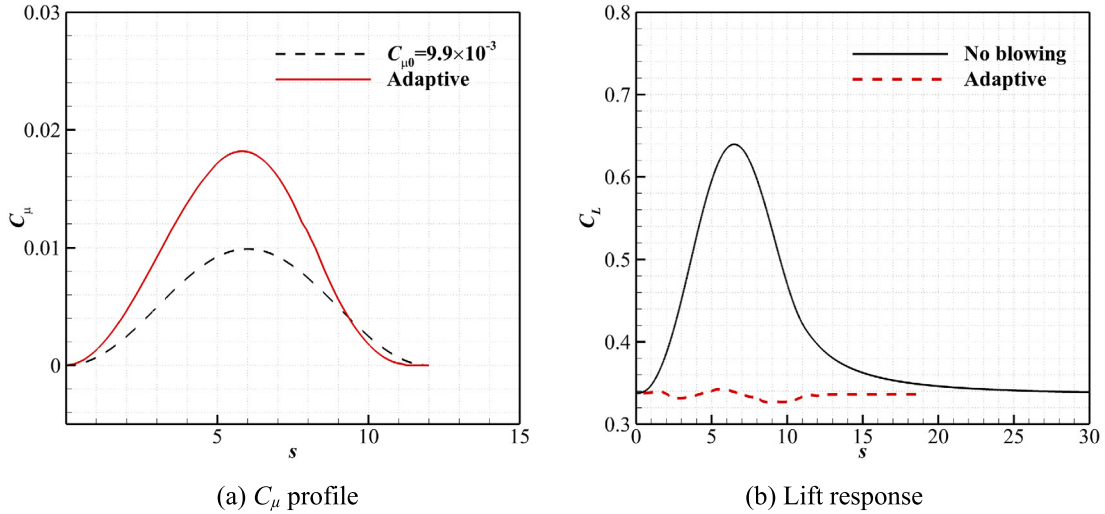


Fig. 22. The gust response using adaptive microjet at $M_\infty = 0.3$.

$$\begin{cases} C_\mu = 0 & s < 0 \\ C_\mu = \frac{1}{2}C_{\mu 0} \left(1 - \cos \frac{2\pi s}{12}\right) & 0 \leq s \leq 12 \\ C_\mu = 0 & s > 12 \end{cases} \quad (5)$$

Fig. 21 shows the gust load alleviations effects. It can be seen that normal microjet has the capability for gust load alleviation. The peak gust-induced lift increment is controlled and further alleviated with the increase in blowing momentum.

In [26], the authors demonstrated the adaptive circulation control for gust load alleviation. Since microjet also has a fast response characteristic, it has a similar capability to control the gust load timely with adaptive characteristics. To test this, the same approach used in [26] is applied here. Based on the data for $C_{\mu 0} = 9.9 \times 10^{-3}$ shown in Fig. 21, the relationship of the lift coefficient reduction caused by microjet named $\Delta C_L(MJ)$ and s relative to $C_\mu(s)$ can be interpolated, which can be expressed as

$$C_\mu(s) = f_1(s, \Delta C_L(MJ)) \quad (6)$$

where, f_1 is the fitting function based on the data of $\Delta C_L(MJ)$, s and $C_\mu(s)$. A quadratic polynomial function is chosen here. Based on this correlation, to compensate the gust-induced lift increment, the required momentum coefficient can be predicted. This process can be treated as an open-loop control. The profile of the predicted momentum coefficients marked as 'Adaptive' is shown in

Fig. 22(a). For the comparison, the momentum coefficients with $C_{\mu 0} = 9.9 \times 10^{-3}$ are also shown in the figure. The time evolution of the lift responses are shown in Fig. 22(b). As shown in the results, the gust-induced lift is better controlled by the adaptive blowing, as a near constant lift response under gust condition is obtained by adaptive microjet blowing. It is true that the adaptive blowing of this study is obtained under a given 'one-minus-cosine' gust perturbation. The designed blowing momentum coefficient profile is tuned for this gust perturbations. In practice, a database of the ability of normal microjet for various momentum coefficients according to different gust velocities and freestream conditions need to be prepared for an open-loop or closed-loop control in a well-designed control system. This case study indicates the capability of normal microjet for adaptive gust load control due to the fast response characteristic and the small 'time-lag' in response.

For a transonic condition, the one-minus-cosine gust with gust velocity of $w_0/U_\infty = 0.033$ and wavelength of $20c$ corresponding to $s = 21$ for the gust to travel past the airfoil, is applied for the freestream flow condition of $M_\infty = 0.7$, $\alpha = 3^\circ$. The unsteady normal microjet with peak momentum coefficients of $C_{\mu 0} = 1.75 \times 10^{-3}$ ($M_{jet} = 0.3$) and $C_{\mu 0} = 4.87 \times 10^{-3}$ ($M_{jet} = 0.5$) are tested. Fig. 23 shows the gust load alleviation effects. It is clear that the peak gust-induced lift increment can be significantly reduced. The lift coefficient after $s = 11$ for the unsteady blowing

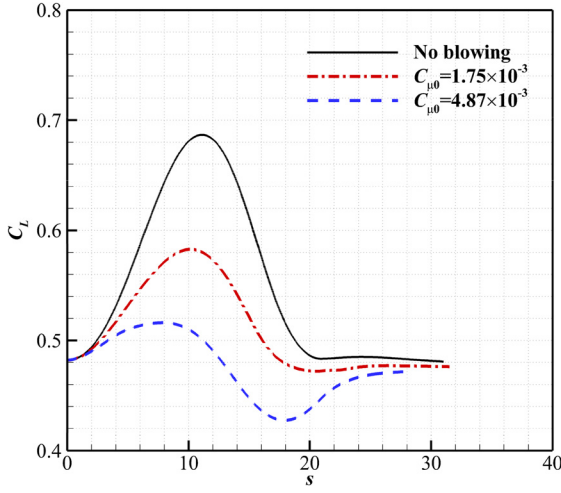


Fig. 23. The gust load alleviation by normal microjet blowing at $M_{\infty} = 0.7$.

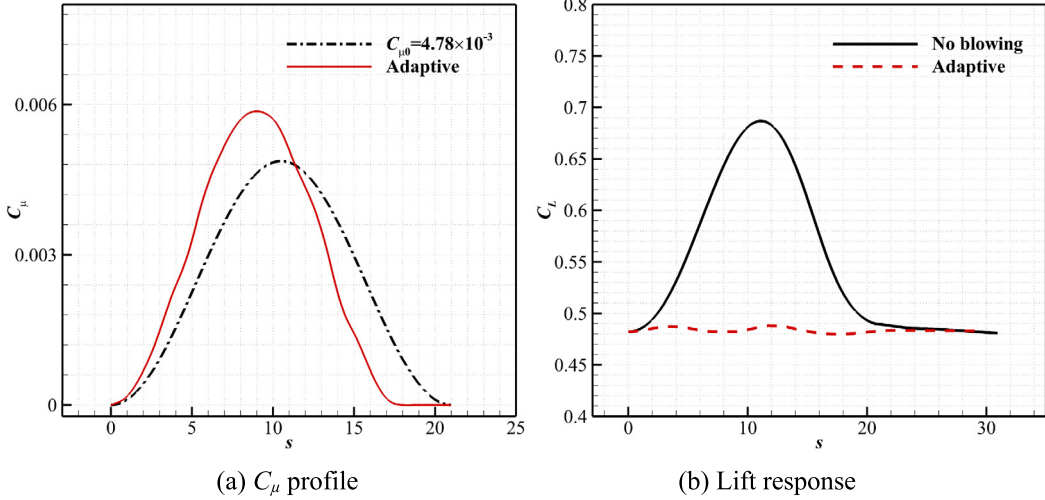


Fig. 24. The gust response using adaptive microjet blowing at $M_{\infty} = 0.7$.

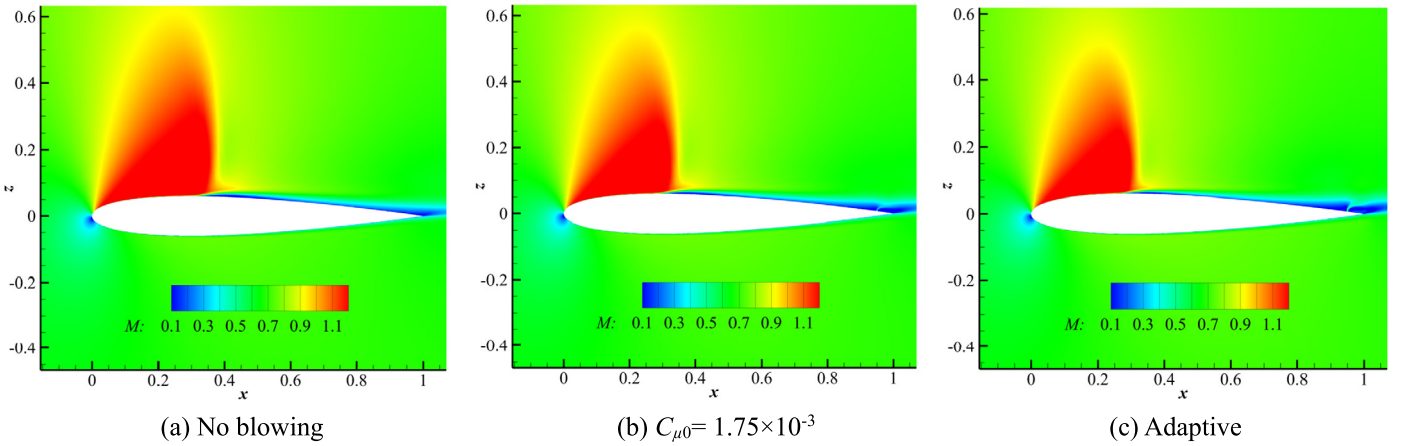


Fig. 25. The Mach number contours at the peak gust load ($s = 11$) for normal microjet blowing.

with $C_{\mu 0} = 4.87 \times 10^{-3}$ is controlled even lower than that of the initial time, indicating a strong load control capability of normal microjet. Based on the data for $C_{\mu 0} = 4.87 \times 10^{-3}$ shown in Fig. 23, the profile of the adaptive momentum coefficients is predicted as shown in Fig. 24. For comparison, the momentum coefficient $C_{\mu 0} = 4.87 \times 10^{-3}$ is also shown in the figure. As expected, the

values of the momentum coefficients after $s = 11$ decrease and the point of the peak value shifts forwards a little due to the 'time-lag' in response. The time evolution of the lift responses is shown in Fig. 24. As shown, the gust-induced lift is completely suppressed by adaptive microjet blowing. Fig. 25 compares the Mach number contours and surface pressure distributions for the baseline model,

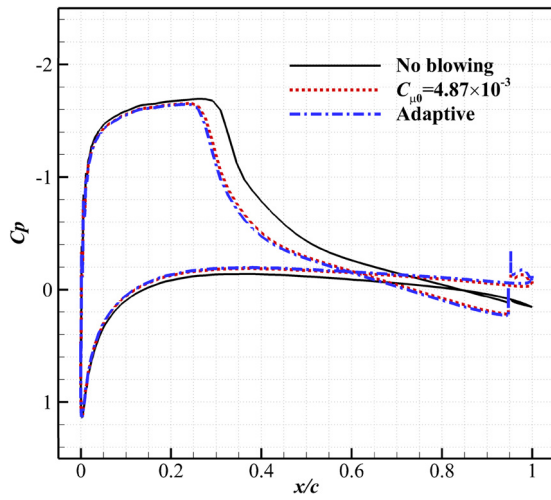
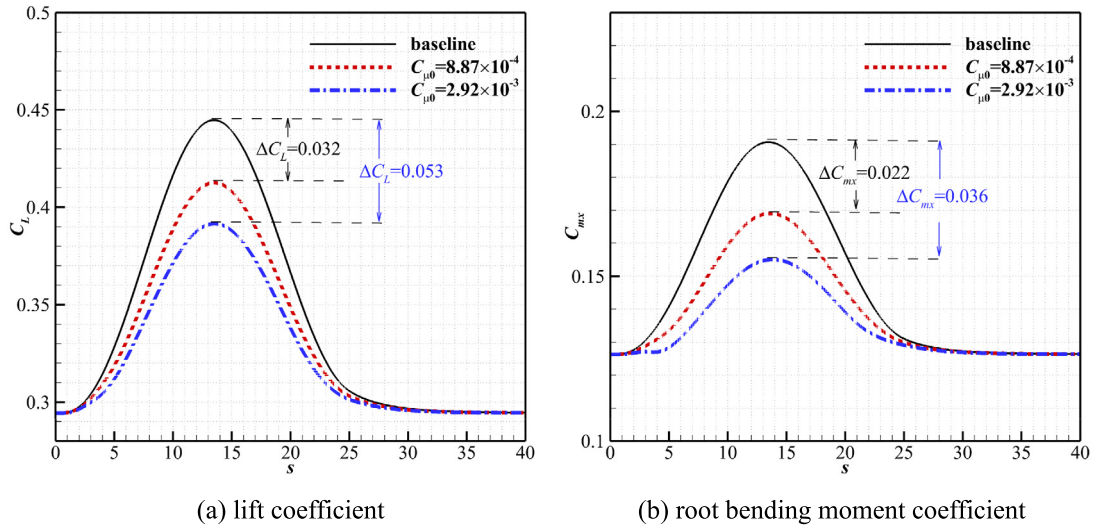


Fig. 26. The pressure coefficient for models with and without CC at peak gust load ($s = 11$).



(a) lift coefficient

(b) root bending moment coefficient

Fig. 27. Load control effects with an unsteady jet blowing under gust condition.

the model with $C_{\mu 0} = 1.75 \times 10^{-3}$ and the model with the adaptive blowing under the peak gust load. Compared to the baseline model, the shock strength is weakened and pushed upstream with the microjet. See also Fig. 26.

These two case studies at subsonic and transonic speeds indicate that normal microjet is capable for gust load alleviation. By timely adjusting the blowing momentum coefficient, it is suitable for adaptive gust control, resulting in complete suppression of gust loads.

5.2. Rigid BAH wing

This 3D wing case tests the gust load alleviation effects on the rigid BAH wing. The gust velocity is set to be 7 m/s ($w_0/U_\infty = 0.029$) corresponding to a gust-induced incidence variation of about 1.6° , and the wavelength of the gust is set to be 100 m (24.2 \bar{C}). The freestream condition is $M_\infty = 0.7$, $\alpha = 3^\circ$. During the simulation, at $s = 0$, the gust hits the leading edge of the root wing section and travels past the wing with the freestream velocity. The momentum coefficients with a 'one-minus-cosine' profile is used for the test, with two different peak momentum coefficients of $C_{\mu 0} = 8.87 \times 10^{-4}$ ($M_{jet} = 0.5$) and 2.92×10^{-3} ($M_{jet} = 0.9$) respectively.

The gust responses in terms of lift coefficient and root bending moment coefficient are shown in Fig. 27. These two unsteady microjets have significant alleviation of the gust loads as shown in the results. To be specific, approximately 21% and 35% of the peak gust-induced lift coefficient is reduced by these two unsteady microjets respectively. A reduction in the peak root bending moment caused by the gust shows to be 34% and 56%, respectively, relative to the baseline model.

5.3. Elastic BAH wing

In this case study, the plunging mode and the first bending elastic mode which are the same as those used in the validation study are included in the gust response simulations. Both the gust and the unsteady momentum coefficients with a 'one-minus-cosine' profile is the same as those used in the previous section.

Fig. 28 shows the resulting time evolutions of the total gust-induced vertical displacement of the leading edge of the wing-tip section. For the baseline model with no microjet, the maximal displacement reaches to 1.35 m caused by the gust load. With the control of microjet, a significant reduction in the vertical displacement is obtained for both blowing cases. To be specific, the maximal displacement reduces to 0.95 m and 0.75 m, respectively for the model with $C_{\mu 0} = 8.87 \times 10^{-4}$ and 2.92×10^{-3} .

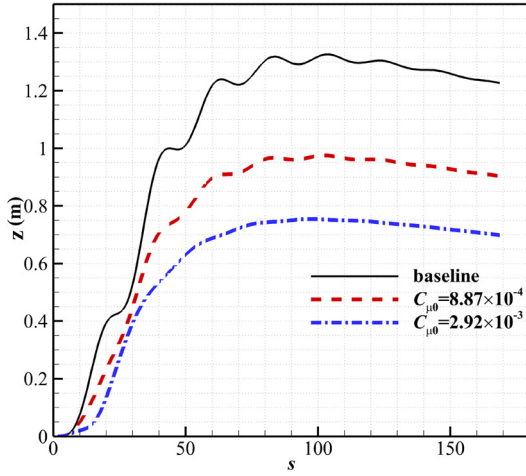


Fig. 28. The total vertical displacement of the leading edge of the wing-tip section.

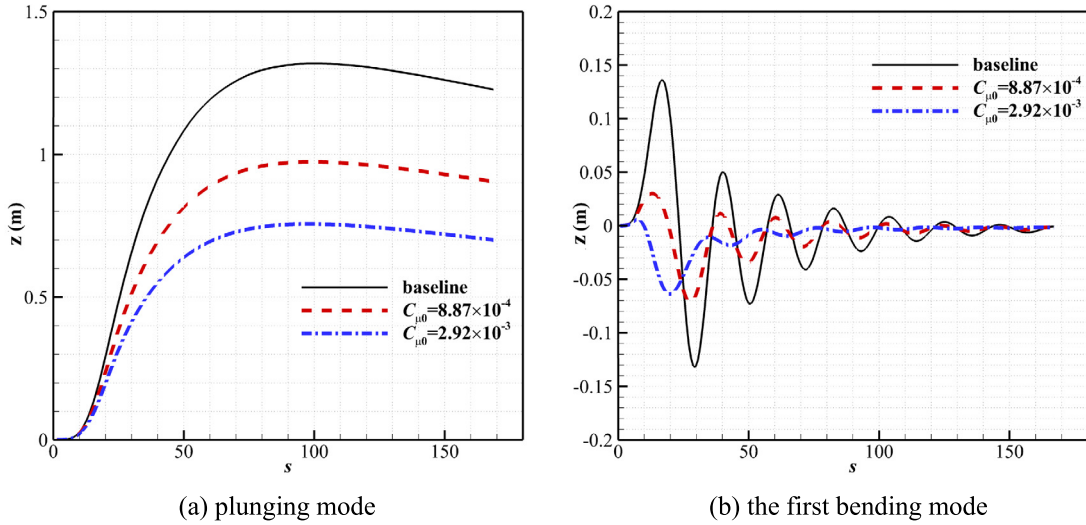


Fig. 29. The vertical displacement of the leading edge of the wing-tip section.

The time evolutions of the individual vertical displacement for the plunging mode and the first bending mode are presented in Fig. 29. Compared to the rigid mode, the displacement of the elastic mode is relatively small. The displacement of the elastic mode is sensitive to the microjet control. For the baseline model, the initial vertical displacement of the elastic mode is upwards due to gust load. When the microjet is deployed with $C_{\mu 0} = 8.87 \times 10^{-4}$, the direction of the initial motion is the same as the baseline model, but with a reduced magnitude due to the alleviation of the gust load. However, when the momentum coefficient increases to 2.92×10^{-3} , the initial motion becomes downwards. The reason is that the gust load on the outer wing sections where microjet slot was deployed experiences significant reduction, resulting in a downward force in the wingtip section. For the baseline model, the vertical displacement of the elastic mode reaches a maximum value of about 0.14 m at $s = 17$, while it is only 0.03 m and -0.05 m for the model with $C_{\mu 0} = 8.87 \times 10^{-4}$ and 2.92×10^{-3} , respectively. The suppression of the wing-tip deformations can be noticed from the comparison of the wing deformations at $s = 17$ as shown in Fig. 30(a). With the gust load alleviation by microjet, the oscillation of the first bending mode displacement decays much faster than the baseline model. Fig. 29(b) shows that the oscillation caused by gust for the model with $C_{\mu 0} = 2.92 \times 10^{-3}$ fades away when s reaches 80. The comparison of the wing deformation

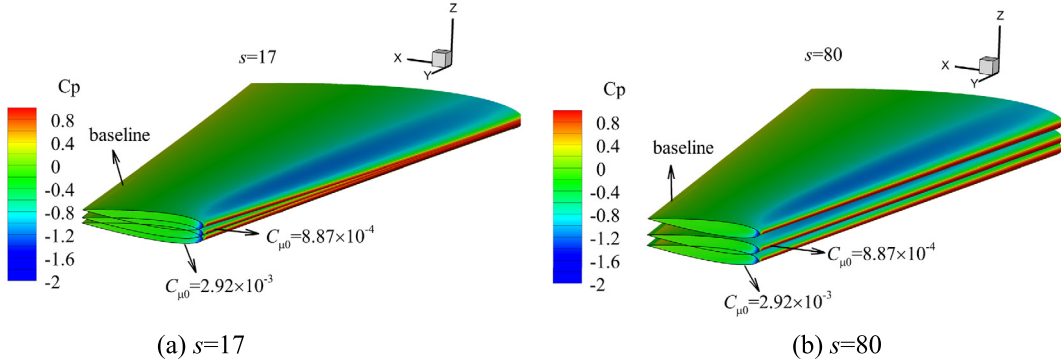
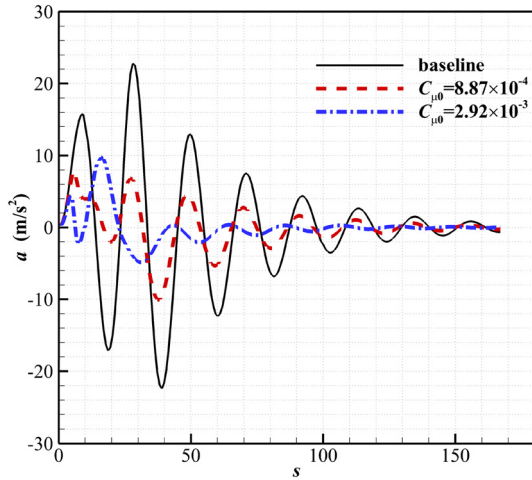
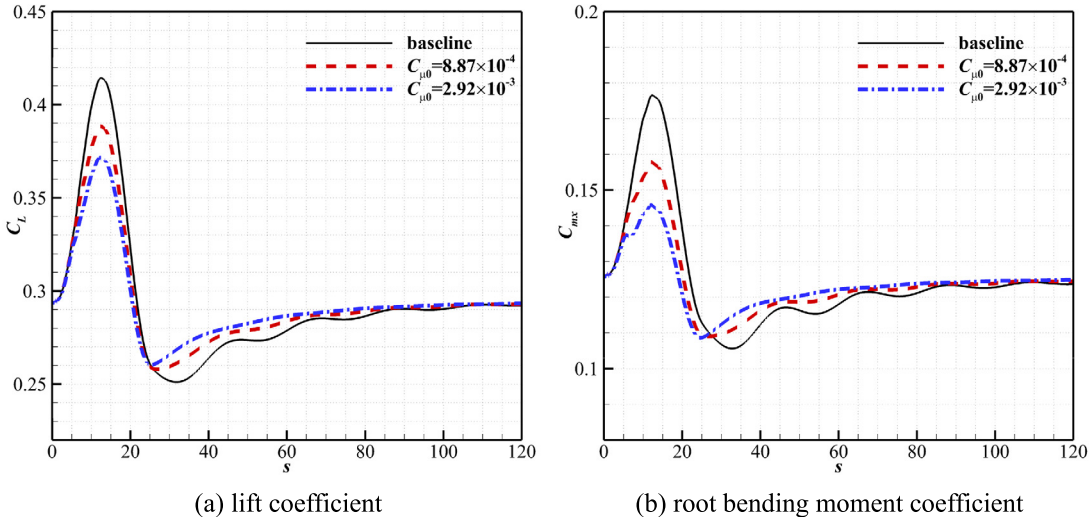
at $s = 80$ is shown in Fig. 30(b), where a significant alleviation on the plunging displacement has been observed.

Fig. 31 shows the time evolutions of the acceleration of the wingtip section in comparison with the baseline model. Significant alleviation of the acceleration due to the gust load has been achieved by the microjet. As expected, the lift and root bending moment are also alleviated which can be noticed in Fig. 32. An alleviation of the peak of 35% due to the microjet with $C_{\mu 0} = 2.92 \times 10^{-3}$ has been obtained on lift, and 60% on root bending moment.

6. Conclusions

The feasibility and effect of gust load alleviation by means of normal microjet are investigated using a numerical method integrating field velocity method, structural dynamic equations of motion and URANS solutions. The method is verified and validated for simulation of gust responses for both rigid and elastic models.

The results show that normal microjet has a stronger load control effect at transonic speed compared to that at subsonic speed with the same blowing momentum coefficient due to the jet effect on shock strength and location. For normal microjet deployed on part of the span near the wing tip, in addition to significant load control effects in the jet deployment region, load reduction has also been obtained on the span region where there is no jet

**Fig. 30.** Pressure distribution and wing deformations.**Fig. 31.** The vertical acceleration of the leading edge of the wing-tip section.**Fig. 32.** The time evolutions of the lift and root bending moment coefficients.

deployment towards the wing root. The results of the dynamic actuation show fast frequency response characteristics as more than 50% of the total change in lift coefficient caused by blowing can be obtained within the non-dimensional time $s = U_\infty t / \bar{c} = 1$.

The results of gust load alleviation on both the airfoil and the 3D BAH wing demonstrate that normal microjet is capable of suppressing the gust load disturbances. Due to the fast response characteristics, timely adaptive gust load control can be achieved. For the test cases of the rigid BAH wing, a significant reduction

in gust-induced lift and root bending moment has been obtained. Because of the alleviation in gust load, significant suppression of the gust-induced disturbances in the displacement and acceleration has been shown in the case study for the elastic BAH wing.

This provides further insights into the feasibility and effects of load control and gust load attenuation by means of normal microjet. Theoretically, the results improved the understanding of the load control capabilities, dynamic response characteristics and the gust load alleviation performance by normal microjet blowing. This

improved understanding can contribute to the design of novel gust load alleviation systems in the future for more efficient and safer transport aircraft for reduced drag and emission.

Declaration of competing interest

The authors declare that they have no known competing financial interests or personal relationships that could have appeared to influence the work reported in this paper.

Acknowledgements

The authors would like to acknowledge the support from the University of Sheffield Computing Service for High Performance Computing provision to conduct the research.

References

- [1] P. Bekemeyer, M. Ripepi, R. Heinrich, S. Götz, Nonlinear unsteady reduced-order modeling for gust-load predictions, *AIAA J.* 57 (5) (2019) 1839–1850.
- [2] S.A. Fazelzadeh, S.M. Jafari, Active control law design for flutter suppression and gust alleviation of a panel with piezoelectric actuators, *Smart Mater. Struct.* 17 (3) (2008).
- [3] X. Liu, Q. Sun, J.E. Cooper, LQG based model predictive control for gust load alleviation, *Aerosp. Sci. Technol.* 71 (2017) 499–509.
- [4] A. Altan, R. Hacıoğlu, Model predictive control of three-axis gimbal system mounted on UAV for real-time target tracking under external disturbances, *Mech. Syst. Signal Process.* 138 (2020) 106548.
- [5] N. Al-Battal, D. Cleaver, I. Gursul, Lift reduction by counter flowing wall jets, *Aerosp. Sci. Technol.* 78 (2018) 682–695.
- [6] N. Al-Battal, D. Cleaver, I. Gursul, Aerodynamic load control through blowing, in: 54th AIAA Aerospace Sciences Meeting, AIAA 2016-1820, 2016.
- [7] Anonymous, BAE systems success in flapless flight, *Aircr. Eng. Aerosp. Technol.* 78 (2) (2006).
- [8] D.T.J. Chan, S. Gregory, William E. Milholen II, Scott L. Goodliff, Transonic drag reduction through trailing-edge blowing on the FAST-MAC circulation control model, in: 35th AIAA Applied Aerodynamics Conference, AIAA AVIATION Forum, AIAA 2017-3246, 2017.
- [9] W. Cui, H. Zhu, C. Xia, Z. Yang, Comparison of steady blowing and synthetic jets for aerodynamic drag reduction of a simplified vehicle, *Proc. Eng.* 126 (C) (2015) 388–392.
- [10] J. Zahn, U. Rist, Active and natural suction at forward-facing steps for delaying laminar-turbulent transition, *AIAA J.* 55 (4) (2017) 1343–1354.
- [11] Z. Guo, M.J. Kloker, Control of crossflow-vortex-induced transition by unsteady control vortices, *J. Fluid Mech.* 871 (2019) 427–449.
- [12] H. Zhang, S. Chen, Q. Meng, S. Wang, Flow separation control using unsteady pulsed suction through endwall bleeding holes in a highly loaded compressor cascade, *Aerosp. Sci. Technol.* 72 (2018) 455–464.
- [13] D. Greenblatt, I.J. Wygnanski, The control of flow separation by periodic excitation, *Prog. Aerosp. Sci.* 36 (7) (2000) 487–545.
- [14] K.S.G. Krishnan, O. Bertram, O. Seibel, Review of hybrid laminar flow control systems, *Prog. Aerosp. Sci.* 93 (2017) 24–52.
- [15] A. Ebrahimi, M. Hajipour, K. Ghamkhar, Experimental study of stall control over an airfoil with dual excitation of separated shear layers, *Aerosp. Sci. Technol.* 82–83 (2018) 402–411.
- [16] M. Amitay, A. Glezer, Role of actuation frequency in controlled flow reattachment over a stalled airfoil, *AIAA J.* 40 (2) (2002) 209–216.
- [17] H. de Vries, C. Boeije, I. Cleine, E. van Emden, G. Zwart, H. Stobbe, A. Hirschberg, H. Hoeijmakers, Fluidic load control for wind turbine blades, in: 47th AIAA Aerospace Sciences Meeting Including the New Horizons Forum and Aerospace Exposition, AIAA 2009-684, 2009.
- [18] N.H. Al-Battal, D.J. Cleaver, I. Gursul, Unsteady actuation of counter-flowing wall jets for gust load attenuation, *Aerosp. Sci. Technol.* 89 (2019) 175–191.
- [19] P. Rao, T. Strganac, O. Rediniotis, Control of aeroelastic response via synthetic jet actuators, in: 41st Structures, Structural Dynamics, and Materials Conference and Exhibit, 2000.
- [20] M. Blaylock, R. Chow, A. Cooperman, C.P. Dam, Comparison of pneumatic jets and tabs for active aerodynamic load control, *Wind Energy* 17 (9) (2014) 1365–1384.
- [21] D. Heathcote, N. Al-Battal, I. Gursul, D. Cleaver, Control of wing loads by means of blowing and mini-tabs, in: European Drag Reduction and Flow Control Meeting – EDRCM 2015, 2015, Cambridge, UK, 2015.
- [22] A.J. Scalfani, M.A. Dehaan, J.C. Vassberg, C.L. Rumsey, T.H. Pulliam, Drag prediction for the common research model using CFL3D and OVERFLOW, *J. Aircr.* 51 (4) (2014) 1101–1117.
- [23] J.W. Edwards, R.M. Bennett, W. Whitlow, D.A. Seidel, Time-marching transonic flutter solutions including angle-of-attack effects, *J. Aircr.* 20 (11) (1983) 899–906.
- [24] V. Parameswaran, J.D. Baeder, Indicial aerodynamics in compressible flow-direct computational fluid dynamic calculations, *J. Aircr.* 34 (1) (1997) 131–133.
- [25] R. Singh, J.D. Baeder, Direct calculation of three-dimensional indicial lift response using computational fluid dynamics, *J. Aircr.* 34 (4) (1997) 465–471.
- [26] Y. Li, N. Qin, Airfoil gust load alleviation by circulation control, *Aerosp. Sci. Technol.* 98 (2020) 105622.
- [27] R.T. Jones, The unsteady lift of a wing of finite aspect ratio, 1940, NACA-TR-681.
- [28] J.R. Wright, Introduction to aircraft aeroelasticity and dynamic loads, in: J.E. Cooper (Ed.), second edition, Wiley, Chichester, West Sussex, United Kingdom, 2015.
- [29] D.E. Raveh, A. Zaide, Numerical simulation and reduced-order modeling of airfoil gust response, *AIAA J.* 44 (8) (2006) 1826–1834.
- [30] R.L. Bisplinghoff, H. Ashley, R.L. Halfman, *Aeroelasticity*, Dover, Mineola, 1996.
- [31] M.S. Corporation, MSC.Nastran Aeroelastic Analysis User's Guide, printed in U.S.A., 2002.
- [32] C. Howcroft, D. Calderon, L. Lambert, M. Castellani, J.E. Cooper, M.H. Lowenberg, S. Neild, Aeroelastic modelling of highly flexible wings, in: 15th Dynamics Specialists Conference, 2016.
- [33] W.P. Rodden, R.L. Harder, E.D. Bellinger, Aeroelastic additions to NASTRAN, Contractor Report 3094, NASA, 1979.
- [34] E. Albano, W.P. Rodden, A doublet-lattice method for calculating lift distributions on oscillating surfaces in subsonic flows, *AIAA J.* 7 (2) (1969) 279–285.
- [35] C.A.A. Eggert, CFD study of NACA 0018 airfoil with flow control, National Aeronautics and Space Administration, Langley Research Center, Hampton, Virginia, NASA/TM-2017-219602, 2017.
- [36] C. Rumsey, Successes and challenges for flow control simulations (invited), *Int. J. Flow Control* (2008) 1–27.
- [37] D. Leopold, A. Krothapalli, D. Tavella, Some observations on the aerodynamics of an airfoil with a jet exhausting from the lower surface, in: 21st Aerospace Sciences Meeting, 1983.
- [38] European Aviation Safety Agency - Certification Specifications for Large Aeroplanes CS-25.